RESEARCH ARTICLE



Check for updates

Scale interactions of deep convection in the Sahel: Exploring ring patterns in lagged cross-correlations of rainfall

James Bassford¹ | Douglas J. Parker^{1,2,3} | John Marsham¹ | James Warner⁴

Correspondence

James Bassford, Institute for Climate and Atmospheric Science, University of Leeds, Leeds, UK.

Email: mm17tjb@leeds.ac.uk

Funding information

Leeds-York-Hull Natural Environment Research Council (NERC) Doctoral Training Partnership (DTP) Panorama under grant NE/S007458/, UK Met Office CASE project funding, and by the LMCS project, Grant/Award Number: NE/W001888/1

Abstract

Spatio-temporal patterns in rainfall are evidence of sub-daily scale interactions in convection in the West African Sahel. Radial normalization of two-dimensional conditional probability maps reveals a ring-like structure in rainfall probabilities surrounding previous rainfall, in both satellite observations and regional climate models. These results support a growing body of evidence that scale interactions in tropical convection can provide predictability on short timescales. Additionally, a km-scale model is shown to represent the spatio-temporal structure of the patterns better compared with the same model at 25 km with parameterized convection. These evaluations indicate the potential for creation or enhancement of statistical prediction tools using model data alongside observations. The mechanism for the patterns is investigated in the km-scale model output, and associations are explored with both convectively generated gravity waves and evaporatively driven cold pools. The area inside the ring-like structure, where the probability of new convection is lower, is associated with a cold and divergent anomaly characteristic of a cold pool. Amplitudes of anomalous mid-level ascent prior to the pattern forming correlate well with amplitudes of the radially normalized probabilities three hours later, suggestive of potential wave-driven enhancement of rainfall probability.

KEYWORDS

climate, convection, interactions, modeling, precipitation, Sahel, scale

1 | INTRODUCTION

The skill of global climate and weather models in predicting both the mean and transient characteristics of tropical rainfall continues to be constrained by the representation of convective processes with distinct characteristic scales, both temporal and spatial (Bony *et al.*, 2015; Cronin & Wing, 2017; Shepherd, 2014; Steiner *et al.*, 2018; Stephan

et al., 2021; Stevens & Bony, 2013). Deep atmospheric convection, which generates strong vertical motion in cumulus towers on horizontal scales $\mathcal{O}(1 \text{ km})$ and smaller, interacts with the surrounding atmosphere via larger-scale coherent structures such as waves, vortices, and density currents. These larger structures can reach the mesoscale, and can then enhance or suppress further convection at these scales. The interaction is clearly two-way and

This is an open access article under the terms of the Creative Commons Attribution License, which permits use, distribution and reproduction in any medium, provided the original work is properly cited.

© 2025 The Author(s). Quarterly Journal of the Royal Meteorological Society published by John Wiley & Sons Ltd on behalf of Royal Meteorological Society.

¹Institute for Climate and Atmospheric Science, University of Leeds, Leeds, UK

²National Centre for Atmospheric Science, University of Leeds, Leeds, UK

³NORCE Norwegian Research Centre AS, Bjerknes Center for Climate Research, Bergen, Norway

⁴Met Office, Exeter, UK

complex, with associated timescales for each of the upscale and downscale components.

Under certain conditions, convection organizes into mesoscale convective systems (MCS). Reviews of MCS dynamics include those of Houze Jr. (2004) and more recently Schumacher and Rasmussen (2020). Through multiple mechanisms, MCS can alter the surrounding dynamic and thermodynamic environment. A synoptic-scale environment containing one or more organized features is then strongly inhomogeneous, and so the probability distribution of otherwise spatially stochastic triggering of new convection can be constrained. More simply, existing convection can enhance or suppress future convection in the vicinity. Two example mechanisms that have been observed to affect both propagation and environmental initiation are convectively generated gravity waves (CGGW) and low-level cold pools resulting from evaporative cooling. The former have been shown to support "gregarious convection", which is observed over the ocean as the multi-scale clustering of clouds (Lane et al., 2001; Lin et al., 1998; Mapes, 1993). Cold pools also play an important role in initiation, by mechanical lifting of air parcels to the point of triggering (Droegemeier & Wilhelmson, 1987; Tompkins, 2001) and through thermodynamic effects (Haerter, 2019; Torri et al., 2015; Trzeciak et al., 2017). The phenomenon of convection determining its own spatial patterns is commonly referred to as self-organization. Convective organization has been the subject of extensive research and review (Mapes, 1993; Moncrieff, 2010; Muller et al., 2022; Stevens, 2005). Understanding how two patterns of rainfall are connected in time through self-organizing mechanisms offers a potential measure of predictability as well as a means of evaluating the physical realism of model processes.

Prediction of convective rainfall requires an understanding of the organizing dynamics, including those of initiation. An example of triggering associated with mesoscale convergence occurs at the low-level gust front of a cold pool or the meeting of multiple cold-pool fronts. Maurer et al. (2017) used a convection-permitting model and found that 35% of initiations of deep convection in the Sahel were triggered by mesoscale convergence at cold-pool gust fronts. These afternoon initiations produce the organized systems that go on to provide nocturnal rainfall. Vizy and Cook (2018) also used a convection-permitting model, in which nocturnal rainfall is most likely sourced from non-orographically initiated MCS. Instead, their proposed initiation mechanisms are a mixture of synoptic-scale moisture gradients and mesoscale circulations.

Land surface feedbacks constrain spatial distributions of the initiation, tracks, and intensity of MCS in the Sahel. In particular, soil moisture is negatively correlated with subsequent MCS tracks and initiation (Klein & Taylor, 2020; Taylor *et al.*, 2011a, 2011b). Gradients of soil moisture can generate density-driven flows, which enhance convection at the edges between wetter and dryer regions (Garcia-Carreras *et al.*, 2011; Taylor *et al.*, 2010). These effects lead to negatively correlated rainfall locations from one day to the next, as the previous day's rain wets the soil, suppressing both new convection and the passage of upstream storms. Birch *et al.* (2013) present a case study where a gravity wave generated by an MCS initiated further convection upon propagating over favorable soil moisture conditions. In this case, convergence was present at the synoptic scale, but the trigger was a combination of mesoscale features.

Spatial patterns in rainfall have practical use in forecasting, as does knowledge of the processes the patterns result from. As part of the Nowcasting FLood Impacts of Convective storms in the Sahel (NFLICS) project (Anderson et al., n.d.; Cole et al., 2022), past observations of MCS convection have been used to build a nowcasting tool that uses a database of location-conditioned probabilities to calculate likelihood maps of near-term future convective activity, based on the current pattern. Methods using proxy observations of soil moisture also show skill in nowcasting the tracks of MCS (Taylor et al., 2022). Other statistical methods have used previous days' rain to predict a day ahead, and this has been shown to outperform a global ensemble in West Africa (Vogel et al., 2021). The skill of the approach is mainly in predicting propagating features, such as MCS and easterly waves (Rasheeda Satheesh et al., 2023; Vogel et al., 2021).

Statistical patterns can also be used to evaluate the extent to which a model has convective memory. Convective memory is defined by Colin et al. (2019) as "the dependence of convective behavior on its own history". In many traditional closure-based parameterizations, memory on convective scales is impossible, given the diagnostic treatment of both the triggering and maintenance of convection. In these regimes, the effects of convection on later convection are only ever felt via changes to the large-scale state variables; the interactions of subgrid-scale processes are absent. By going to higher resolutions, models can begin to resolve memory-carrying features, such as cold-pool gust fronts, explicitly. However, there have also been efforts to develop cold-pool schemes using subgrid and cross-column prognostic variables and equations, which can be coupled to convective diagnosis (Freitas et al., 2024; Grandpeix & Lafore, 2010; Rio et al., 2009; Rooney et al., 2022).

Rainfall in West Africa, and across the Tropics more broadly, is inherently unpredictable at a 1–7 day lead time (Keane *et al.*, 2025). At the same time, near-term information about rainfall is critical to local livelihoods and

flood vulnerability. There is therefore a need to quantify spatio-temporal patterns in rainfall better at shorter, sub-daily timescales. These sub-daily patterns can then be used to evaluate models, assess their value for short-range prediction, and understand better the associated physical processes and how model errors may relate to these. This study identifies novel spatio-temporal patterns of rainfall that provide predictability on the sub-daily timescale. We show these patterns exist in both observations and a climate model, and link them to well-studied dynamical processes. We present examples of using the patterns for novel model evaluation, comparing the results from observations with those from a regional climate model with both explicit convection and parameterized convection. In the next section, we discuss the data used and the methods of pattern construction. Then we present results relating rainfall to rainfall at a later time, and then those relating rainfall to other model fields at a later time. The latter relationships are chosen to explore associations between time-lagged patterns in rainfall and mechanisms of convective initiation, gravity waves and cold pools. We then finish with a discussion of sensitivities of the method in the context of storm life cycles and the potential applications of quantifying these patterns, such as the development or improvement of nowcasting tools.

2 | METHODS

2.1 | Data

The model data used in this study are from the Improving Model Processes for African Climate (IMPALA) project (Stratton *et al.*, 2018). We use two custom configurations of the Met Office Unified Model, one with explicit convection at 4.5-km resolution (CP4), and another with parameterized convection at 25 km (P25). In June, July, and August (JJA) in West Africa, P25 has a seasonal dry bias relative to satellite retrievals of rainfall. CP4 has a smaller but still negative seasonal bias and a higher frequency of higher rain rates, but produces too much rain over steep terrain. CP4 also has a better representation of land-based MCS over the region, particularly of long-lived and fast-moving storms (Crook *et al.*, 2019). See Stratton *et al.* (2018) for more detail on general rainfall biases and Crook *et al.* (2019) for details of MCS represenation.

We perform analysis on data from 1998 to 2006 for June–September inclusive. This gives us nine years of 120-day seasons, giving a total of 1080 days of data for both CP4 and P25. The model fields used are hourly rainfall rates and three-hourly winds, temperature, and pressure tendency (omega). All variables are instantaneous. We compare the models with satellite-based retrievals

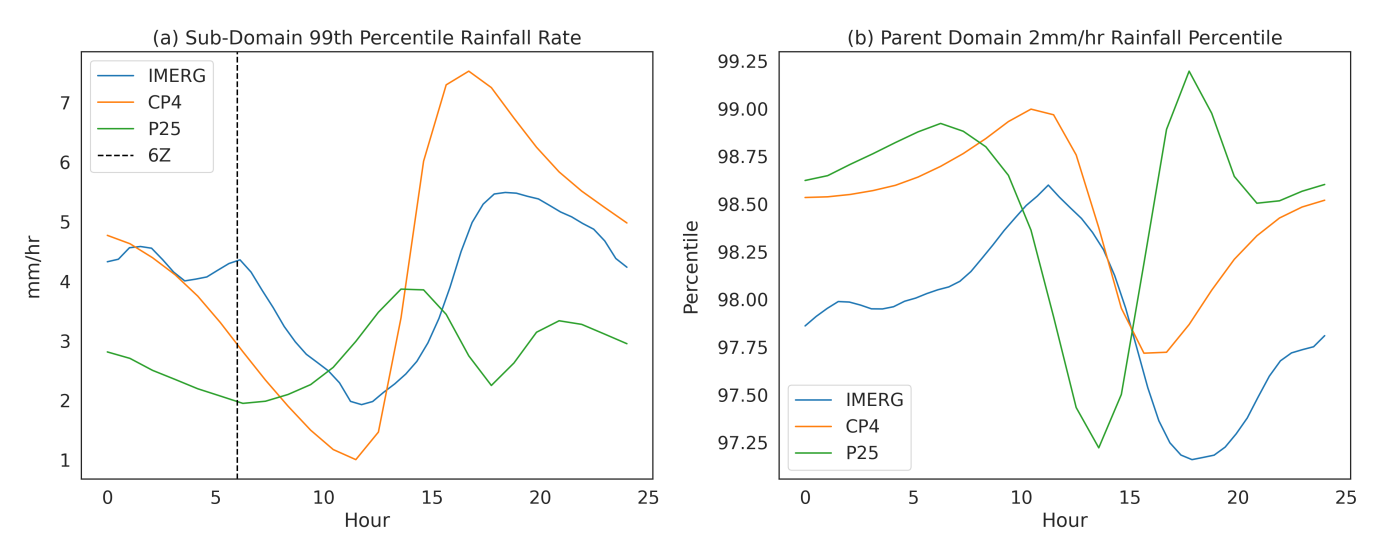
of rainfall rate from *Global Precipitation Measurements* (*GPM*) Integrated Multi-satellitE Retrievals (IMERG) version 6 (Hou *et al.*, 2014), which are on a 0.1° grid that approximates a 10-km resolution in the analysis domain.

The analysis domain here is in two parts, a parent and a sub-domain. The parent domain is from 16°W-16°E and 2°N-26°N, which encompasses the majority of the land surface of tropical West Africa and some adjacent ocean. It is worth remembering throughout that UTC is approximately LST in this domain, given the importance of diurnal cycles for convective rainfall. The sub-domain is the Western Sahel from 8°W-8°E and 10°N-18°N. This sub-domain was chosen to be entirely continental, to minimize coastal effects, and to minimize the presence of significant orography. A higher proportion of the largest and longest-lived systems also develop in the chosen sub-domain (Lafore et al., 2017). These large systems produce the most intense updrafts and rainfall and are often active through the night. The parent domain is 8° larger in all directions than the sub-domain, with a common center at (0°, 14°N). The parent domain includes both the south and west coasts of tropical West Africa as well as both inland and coastal areas of significant orography, the implications of which are discussed later.

2.2 | Lagged cross-correlations

Cross-correlations were calculated between the sub-domain high rainfall locations at time t_0 and the parent-domain convective rainfall locations at t_1 . High here refers to rainfall above the t_0 99th percentile for the sub-domain, relative to the respective climatology of the data source. At t_1 , a threshold of 2 mm/h is chosen simply as a representative rain rate for convection. Using percentiles at t_0 samples similar numbers of t_0 events in each data source. At t_1 , the primary concern is the differences between the models and between models and observations. Figure 1a shows how the t_0 thresholds change through the diurnal cycle in the sub-domain and Figure 1b shows how much rain > 2 mm/h one might expect in the parent domain for each model throughout the day. By using a fixed t_1 threshold, we clearly keep the diurnal cycle biases of the models in the results, highlighting their leading-order impact on the timing of the development of spatial structure.

Cross-correlations were also calculated between high rainfall at t_0 and anomalies of temperature, horizontal winds, and omega at t_1 . The anomalies are defined as deviations from the 10-year grid cell mean for a given time of day and pentad. All cross-correlations were calculated for a range of t_0 and t_1 values, but for clarity the choice was made to restrict the majority of the discussion to the results



Mean diurnal cycles of the thresholds used to define t_0 rain event and t_1 convective rain locations. (a) The sub-domain 99th percentile rainfall values at all possible t_0 for CP4, P25, and IMERG. (b) The percentile corresponding to 2 mm/h at all possible t_1 for CP4, P25, and IMERG. [Colour figure can be viewed at wileyonlinelibrary.com]

of cross-correlations with a fixed t_0 of 6Z (Z indicates Coordinated Universal Time or UTC), for which signals were strongest. The evolution of the patterns with increasing lag time (i.e., by advancing t_1) then gives patterns in rainfall throughout the day relative to rainfall locations at 6Z. The highest rainfall at 6Z is often found in long-lived nocturnal MCS.

First, the rainfall field (in mm/h) is passed through a Heaviside function to create a binary array that is one where rainfall is above the threshold and zero elsewhere. This is done separately for the parent and sub-domain with their respective thresholds. For t_1 temperature and wind anomalies, the Heaviside is not applied. The cross-correlation is then calculated using the standard "signal.correlate" method in the signal-processing library from the open-source SciPy Python package. We make use of the built-in fast Fourier transform (FFT) option to speed up the calculation. We also use the built-in option to trim the edges of the full cross-correlation to the size of the parent domain, keeping the center the same. Because the sub-domain and parent domain have a common center, the center of the resulting cross-correlation represents the location of a t_0 event, which will be labeled as the origin. An example is illustrated in Figure 2 for a single day of data with $(t_0, t_1) = (6Z, 15Z)$.

For a start time t_0 , a set of cross-correlations is calculated for each lag time $t_1 - t_0$. Dividing each cross-correlation by the total number of rain events in the t_0 domain gives a conditional probability map. This map shows the probability of rain at (x, y, t_1) , given high rainfall at $(0, 0, t_0)$. This calculation is repeated for each day in the June, July, August, September (JJAS) period of each year from 1998 to 2006, giving a total of 1080 cross-correlations

for each lag time. Taking point means over all 1080 cases gives one final set of probabilities for each lag time. In the following results, $t_0 = 6Z$ in all cases.

The distance of maximum probability from the average t_0 rain location for a given radial direction can be found by transforming into polar coordinates (r, θ) and normalizing the correlation values in each of $2\pi/\alpha$ sectors of a domain-wide circle around the origin, for a small angle α . This shows, for each θ independently, where on the radius the highest probabilities are located. This approach highlights radial structures when changes in the intensity of the signal with angle make the patterns otherwise harder to perceive. In this case, $\alpha = 0.5^{\circ}$ is used and the values are normalized in [0, 1]. We are then able to identify whether coherent radial structure exists, in which the higher values of probability in a given direction are found at similar distances from the t_0 rain location.

RESULTS

Lagged rainfall to rainfall cross-correlation

Figure 3 shows the mean conditional probability maps between sub-domain rainfall at 6Z and the parent domain at three-hourly intervals. All three datasets show an area of high probability propagating in a west-southwest (WSW) direction. This direction is known to be the dominant climatological propagation direction for Sahelian squall lines (Crook et al., 2019; Mathon et al., 2002; Tulich & Kiladis, 2012). By visual inspection, the shape and propagation of these areas in the CP4 map are more similar BASSFORD ET AL. Quarterly Journal of the RMetS 5 of 15

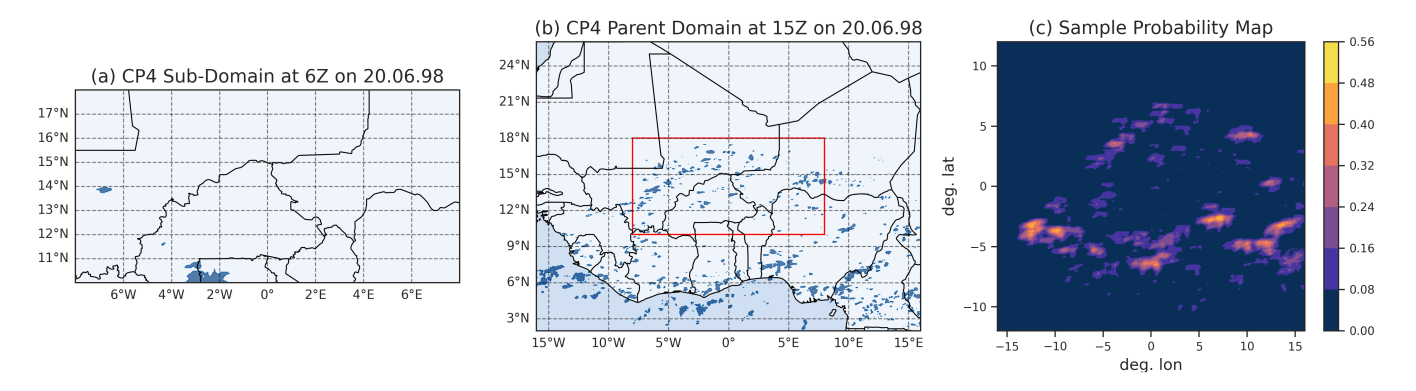


FIGURE 2 An example of a probability map derived from cross-correlation (c) for a single day with $t_0 = 6$ Z and $t_1 = 15$ Z. Locations with rainfall over the thresholds are shaded blue in (a) and (b). The sub-domain (a) is shown in (b) by the red rectangle. [Colour figure can be viewed at wileyonlinelibrary.com]

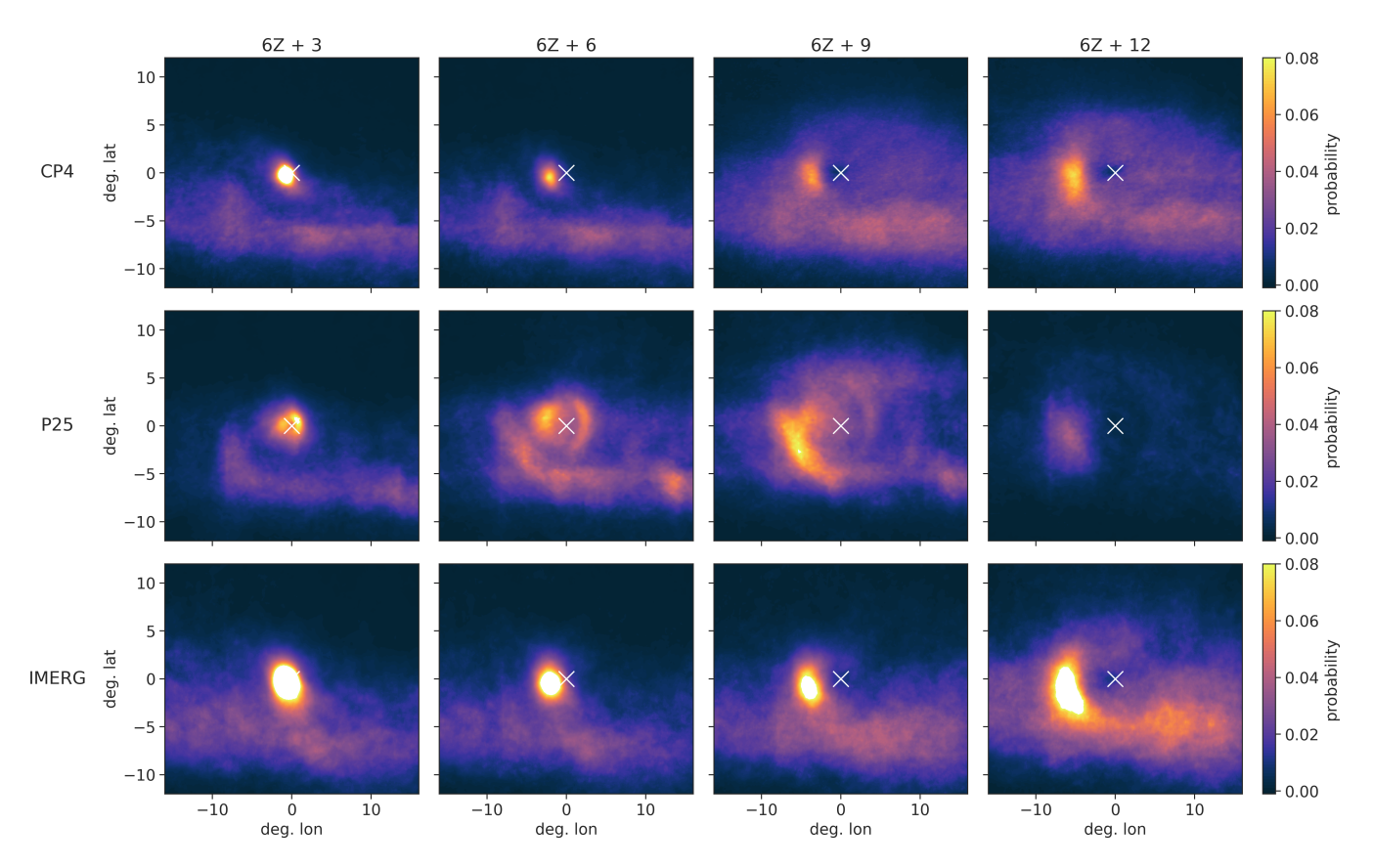


FIGURE 3 Probability of rain > 2 mm at t_1 , surrounding the mean 99th percentile 6*Z* rain location, with $t_1 = 9Z$, 12*Z*, 15*Z*, 18*Z* for CP4, P25, and IMERG. See Section 2.2 for the calculation method. [Colour figure can be viewed at wileyonlinelibrary.com]

to those in observations than those in P25. The P25 map also shows an additional east–northeast (ENE) moving feature, which is not consistent with known climatologies. These model differences are consistent with previous work comparing organized convective rainfall in CP4 and P25 (Crook $et\ al.$, 2019). In both CP4 and IMERG probability maps, there are stationary features associated with orography to the southeast (SE) for +6 to +12. The feature is likely associated with climatological orographic rainfall in the

Jos Plateau, approximately (10N, 8E), and the mountains of northwestern Cameroon and southwestern Nigeria.

In Figure 4, differences in spatial maximum probability are due to a combination of model rainfall biases and resolution. Probabilities are generally higher in the IMERG map at all lag times than for both models. By using a fixed threshold at t_1 , the time evolution of the mean probability follows closely the diurnal cycle of the 2 mm/h percentile shown in Figure 1. However, the evolution of

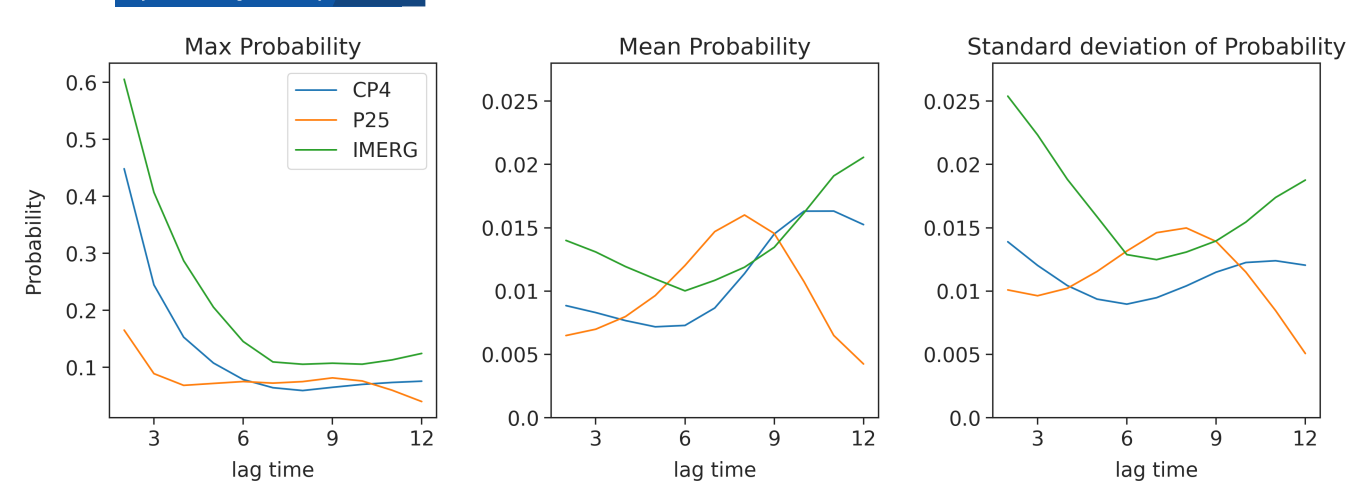


FIGURE 4 Maximum, mean, and standard deviations of the probabilities (*P*) in Figure 3. [Colour figure can be viewed at wileyonlinelibrary.com]

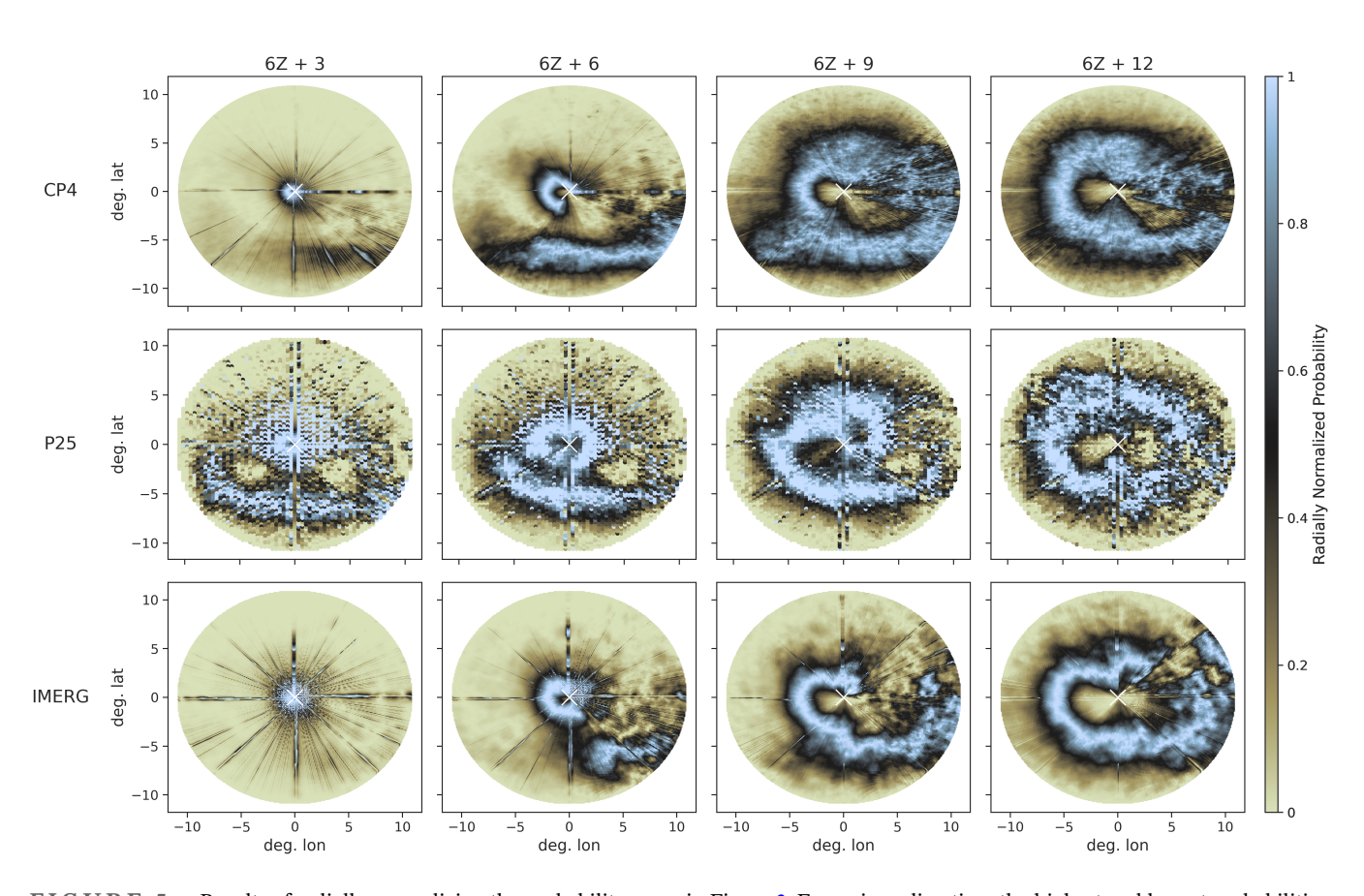


FIGURE 5 Results of radially normalizing the probability maps in Figure 3. For a given direction, the highest and lowest probabilities are represented in pale blue and brown, respectively. See Section 2.2 for calculation details. [Colour figure can be viewed at wileyonlinelibrary.com]

the spatial variability in CP4 probabilities is also closer to observations. The improved mean diurnal cycle is a known advantage of convection-permitting simulations more generally (Birch *et al.*, 2014; Stratton *et al.*, 2018).

Figure 5 shows the same data as Figure 3, but each probability map has been normalized radially using the

method described previously. The result is a coherent ring-like structure of higher values around the t_0 location of convection. The rings are of similar size for all data sources, with an average radius of 600 km at a lag of +12 hours. Considering the ring as growing with time, the average propagation speed is approximately $14 \,\mathrm{m} \cdot \mathrm{s}^{-1}$.

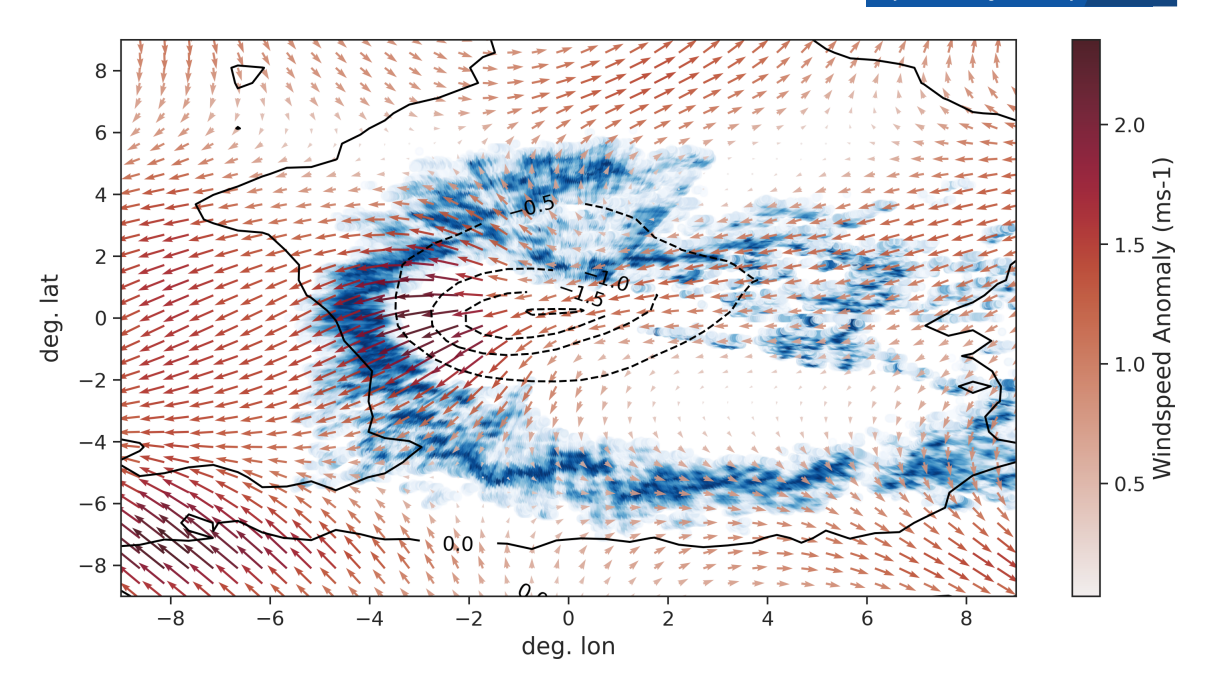


FIGURE 6 Mean CP4 cross-correlation of 6Z rainfall locations over the threshold with $t_1 = 12Z$ 925-hPa temperature anomalies in K (black contours) and 925-hPa horizontal wind anomalies (arrows). Blue shading shows the top 20% of the radially normalized rainfall probabilities at $t_1 = 15Z$. [Colour figure can be viewed at wileyonlinelibrary.com]

This is faster than the modal range of MCS propagation in both models and observations, which ranges from $4-12\,\mathrm{m\cdot s^{-1}}$ depending on the model or observations (see fig. 6a of Crook *et al.*, 2019). However, $14\,\mathrm{m\cdot s^{-1}}$ is well inside the observed spread. Patterns in Figure 5 for CP4 and IMERG are more similar, particularly up until +9 h. A tight range of radii for the highest values of the radially normalized probabilities is common to all at lag +12. For CP4 and IMERG, there are clear local minima close to and west of the origin, and the pattern becomes much noisier to the east. The pattern in P25 at +12 is generally more zonally symmetric, including in the central minimum.

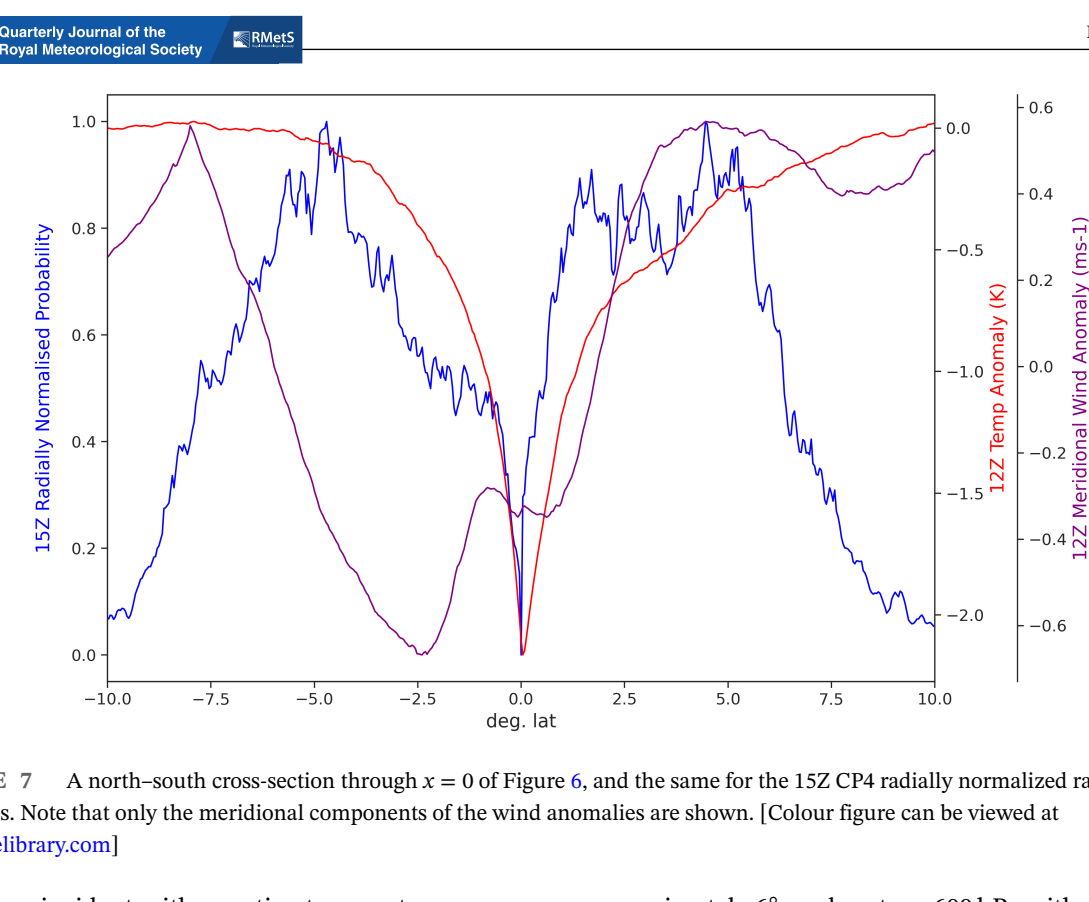
3.2 | Investigating physical mechanisms

In testing for organizing mechanisms, we will therefore continue to use data from the CP4 model, based on its better agreement with IMERG in Figures 3 and 5, whilst remaining aware of the temporal differences seen in Figure 4. Since the rings in Figure 5 have some radial thickness, we assume a range of propagation speeds exist in the associated mechanisms. The speed of ring "growth" can be used to begin to determine which parts of the pattern are potentially associated with cold pools and which with waves. We can first use a cross-correlation of 6Z rainfall with t_1 temperature and wind anomalies to determine the likely location of cold-pool gust fronts.

Figure 6 shows the nine-season mean cross-correlation of 6Z high rainfall locations with $t_1 = 12Z$ temperature

(contours) and meridional wind anomalies (arrows) at 925 hPa. Overlaid in blue are the values of the highest 20% of the radially normalized probabilities for three lag hours later at $t_1 = 15Z$. This is done to make $t_1 = 12Z$ the pre-rain environment. Again the origin represents the location of the 6Z high rainfall. The temperature and wind cross-correlation values have been divided by the number of high rain points at t_0 : this gives an estimate for the mean magnitudes of the anomalies. At 12Z, there is an elliptically shaped mesoscale cold anomaly centered just westward of the intense rainfall location six hours prior. The majority of high values in the 15Z radially normalized probabilities are found at the edge of the cold anomaly between the -0.5 K and 0 K contours. The wind anomalies near the origin show a component of divergent flow outward from the earlier rain location, except to the east. In many places there is convergence of the wind anomalies where we find high values of the radially normalized probabilities three hours later. The western part of the pattern is reminiscent of cold outflow-driven lifting ahead of a propagating MCS. To the north, however, a propagating storm does not explain the ring location, so we will next examine just a cross-section of the pattern.

Figure 7 shows a north–south cross-section of Figure 6. Overlaid now are all the values of the radially normalized probabilities on that cross-section for $t_1 = 15$ Z. The cross-section is chosen to mostly exclude the propagating "MCS" itself and focus instead on the surrounding environment. The maximum magnitude of the wind



A north-south cross-section through x = 0 of Figure 6, and the same for the 15Z CP4 radially normalized rainfall probabilities. Note that only the meridional components of the wind anomalies are shown. [Colour figure can be viewed at wileyonlinelibrary.com

anomalies coincident with negative temperature anomalies in this cross-section is $< 1\,\text{m}\cdot\text{s}^{-1}$. If this speed were maintained, it would give a radius of < 100 km (or 1°) in 12 hours. This is a conservative estimate, since not every event used to construct the average will have a strong cold pool, bringing down the average magnitude of the anomalies. Using instead the JJAS composite cold-pool front speed of $6.5 \,\mathrm{m\cdot s^{-1}}$ in Provod et al. (2016) gives an estimated radius of < 300 km (or 3°) in 12 hours. The sections of the rings to the north and south extend as far as 600 km from the average 6Z rain point. These more distant correlations are more likely the result of faster cold-pool gusts or gravity waves, as seen in Birch et al. (2013). Meridional asymmetry is present in both the temperature and wind anomalies. The mean cold anomaly extends further north than it does south, potentially because a given expanding pool of cold air at a given temperature will be more negatively anomalous in the warmer north. These asymmetries could also be due to contrasting boundary-layer characteristics that favor more or less cold-pool propagation.

Next, we search the same cross-sections for the presence of wave-like signals in anomalies of vertical motion. Figure 8 shows two latitude-height sections of the mean cross-correlation of 6Z rainfall with omega and meridional wind anomalies between 925 and 100 hPa, where $t_1 = 9Z$ (left) and 21Z (right). At 9Z, positive/negative omega anomalies (descending/ascending air) dominate the lower/upper column in the area surrounding the 6Z rain event. 12 hours later, at 21Z, a region of weak descent extends northward from the 6Z rain location

approximately 6° , and up to $\sim 600 \, \text{hPa}$ with ascent above. The vertical structure to the north is similar to that associated with stratiform heating (Houze Jr., 2004; Schumacher et al., 2004; Schumacher & Houze, 2006), with upper-level ascent and lower-level descent. Combined with the deep ascent seen to the south, this would be the expected contribution to the signal from a southwesterly propagating MCS with a trailing stratiform region. Figure 9 is another cross-section, this time of the 12Z 500-hPa omega anomaly cross-correlations alongside the subsequent 15Z radially normalized probabilities. The amplitudes of the two are clearly out of phase to distances of 6-7°.

DISCUSSION

Summary of results

A coherent ring-like pattern of higher conditional probabilities of rainfall around earlier rainfall is accentuated by normalizing radially. The rings have a scale of \sim 1000 km at a lag time of t_0 + 9-12 hours and include a region of high probability to the west of the earlier rainfall, indicative of MCS propagation. The patterns calculated from a model with explicit convection show spatial and diurnal cycle characteristics more similar to those in observations, compared with a model with parameterized convection. We present statistical indications that convective memory may contribute to improved diurnal cycles—an improvement noted in previous studies of convection-permitting models.

rary.wiley.com/doi/10.1002/qj.70041 by University Of Leeds

Wiley Online Library on [28/10/2025]. See the Terms

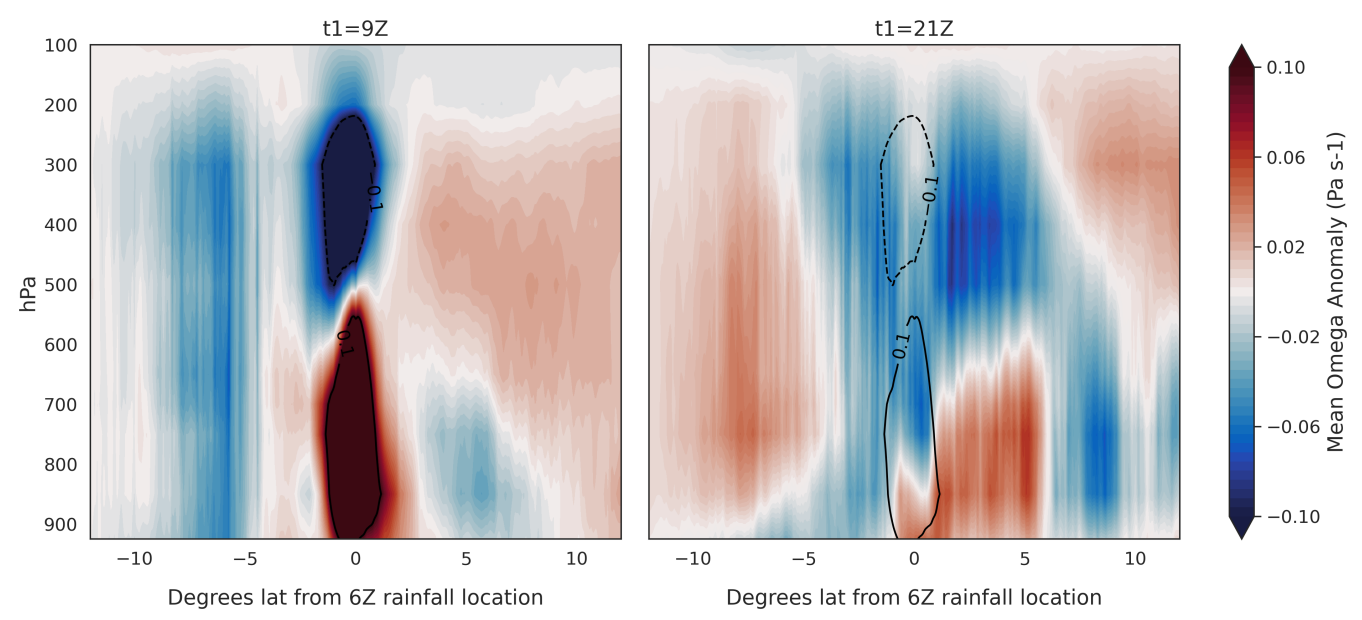
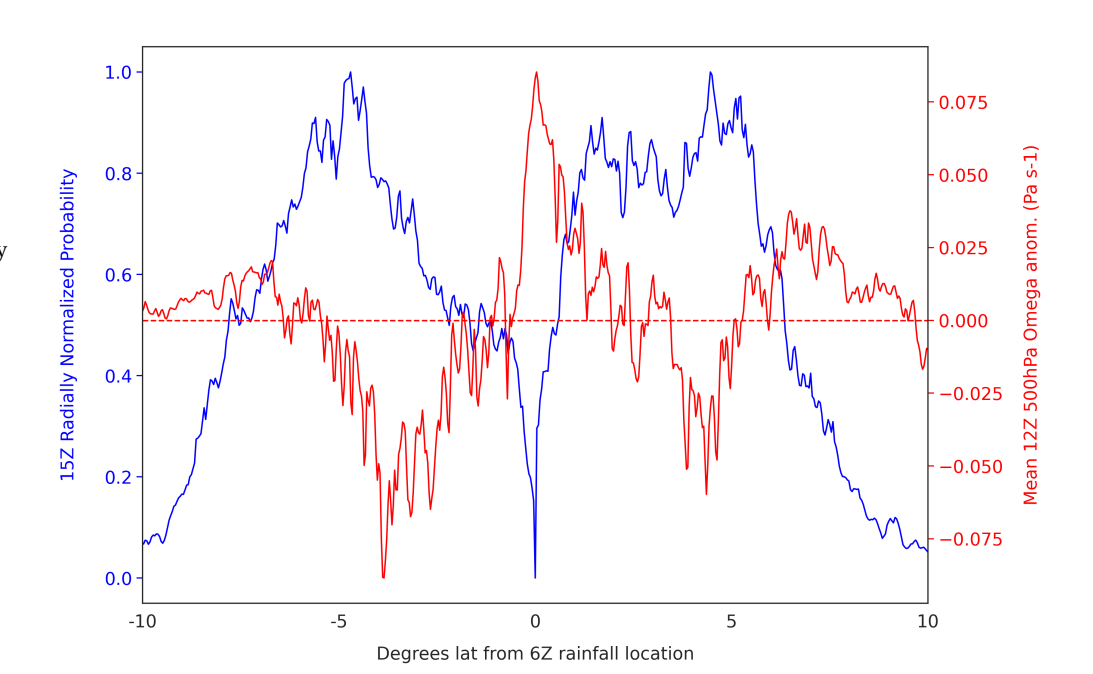


FIGURE 8 A latitude-height cross-section through x = 0 of the mean CP4 rainfall and omega anomaly cross-correlation with $t_0 = 6$ Z and $t_1 = 9$ Z and 21Z. On both panels the ± 0.1 Pa · s⁻¹ contours are shown for $t_1 = 9$ Z. [Colour figure can be viewed at wileyonlinelibrary.com]

FIGURE 9

A north–south cross-section through x = 0 of the CP4 rainfall and omega anomaly cross-correlation (red) with t_0 , $t_1 = 6$ Z, 12Z. In blue is the cross-section of the CP4 radially normalized probabilities for $t_1 = 15$ Z. [Colour figure can be viewed at wileyonlinelibrary.com]



The mechanisms for coherent patterns are explored in the convection-permitting model, and we find patterns in the dynamics with features common to cold pools and gravity waves. Cold pools are identified by anomalously cold and divergent regions at time t_1 , around where convective rainfall occurred at time t_0 . At the edge of these regions, anomalous convergence leads to an enhancement of the radially normalized probabilities, particularly in the western half of the coherent pattern. Cross-sections through composite cross-correlations of rainfall with vertical motion show that 12Z anomalies in 500-hPa ascent are anti-correlated with 6Z, rain locations

but correlated in a region 2–6° away. This ascent is co-located with the peaks in a similar cross-section of the radially normalized probabilities.

4.2 | Start time sensitivity and storm life cycles

As mentioned in Section 2, the choice of start time used in the cross-correlations (CC) was dictated by which produced the strongest correlations not attributable to stationary features such as coasts and orography. However, this is not to say that starting at other times does not

elibrary.wiley.com/doi/10.1002/qj.70041 by University Of Leeds Brotherton, Wiley Online Library on [28/10/2025]. See the Terms and Conditions (https:

ms) on Wiley Online Library for rules of use; OA articles are governed by the applicable Creative Commons I

1477870x, 0, Downloaded from https://rmets.onlin

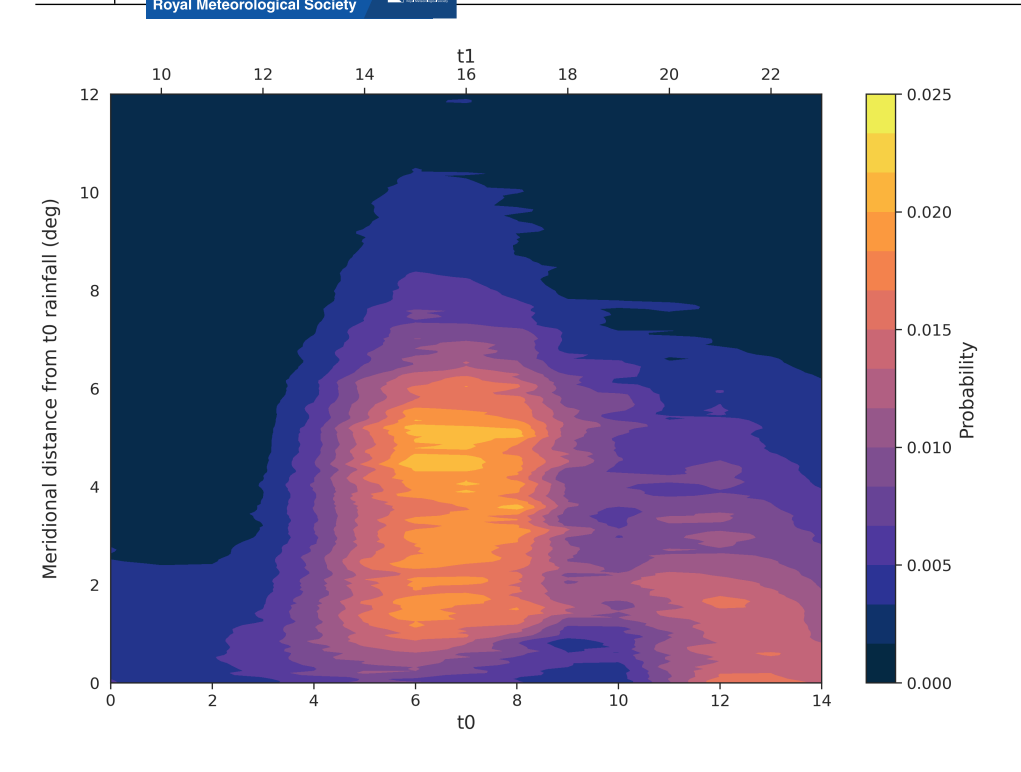


FIGURE 10 Sections of probability maps at $t_0 + 9 \, \mathrm{h}$ for t_0 in 0,14Z. Only the northward direction from the mean t_0 rainfall location is shown for simplicity. Meridional distance northward from the origin is shown by the *y*-axis. The lower *x*-axis shows t_0 and the upper *x*-axis is the corresponding $t_1 = t_0 + 9 \, \mathrm{h}$. [Colour figure can be viewed at wileyonlinelibrary.com]

produce coherent patterns. To quantify the sensitivity of the method to start time, we can calculate the mean CC for the full range of t_0 , all with a fixed lag time. Taking one-dimensional cross-sections of the resulting arrays and stacking them along a common axis shows us the distribution of conditional probabilities in (t_0, D) space, where D is the distance from the mean t_0 rain point as in the figures in Section 3.

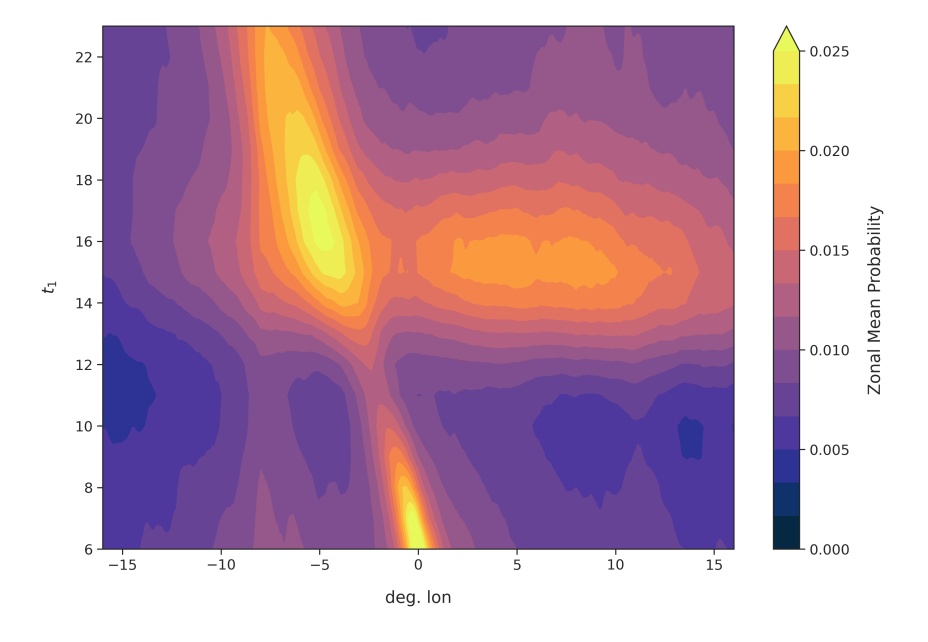
The (t_0, D) space plot gives us information about both the amount and the speeds at which t_0 rain enhances t_1 rain in the surrounding area. Figure 10 shows such a plot for northward cross-sections of CC with t_0 from 0 to 14Z, all with a fixed lag of 9 h. As such, the corresponding t_1 are from 9Z on the same day to 23Z. We can interpret this under the assumption that higher probability results from some propagating response of the atmosphere to t_0 rainfall after 9 h. For example, a significant correlation at 5° north corresponds to some propagating feature that travels at $\sim 17 \,\mathrm{m\cdot s^{-1}}$. We see the strongest correlation at distances requiring speeds between ~ 5 and $20 \,\mathrm{m}\cdot\mathrm{s}^{-1}$ when t_0 is 5–8Z, and only up to $\sim 10 \,\mathrm{m\cdot s^{-1}}$ for t_0 of 12–14Z. All these speeds can be achieved by cold-pool gust fronts (Provod et al., 2016) or gravity waves, other than the first baroclinic mode, which is much faster.

Fast moving gust fronts and large-amplitude gravity waves are generated by large buoyancy perturbations in MCS. The slower speeds for afternoon t_0 could be the result of local clustering of new afternoon initiations around surface features (Garcia-Carreras *et al.*, 2011) or enhancement by slower gust fronts generated in smaller storms (Meyer & Haerter, 2020). The afternoon boundary

layer is less stable, and so does not allow for as fast a propagation of waves along its top as could be possible at night or in the early morning. At 5-8Z, the likelihood of initiation of new isolated convection and subsequent generation of CCGW is low (Fink et al., 2017). We assume that any intense rainfall at these times is from existing MCS that have been maintained through the night. The impact of the collapse of MCS in the morning on the subsequent afternoon initiations could be a potential explanation for the significance of the 5–8Z choice of t_0 . Similarly to how initiation is associated with CCGW, collapse should also generate similar waves, but with the opposite phase. Storm collapse will also be associated with mesoscale subsidence, low-level evaporative cooling, and soil-moisture feedbacks. All these arguments support suppression of convection in storm collapse regions, with enhanced convection at the interface with the surrounding environment. These long-lived nocturnal storms are more common in the chosen sub-domain than further to the south (Lafore et al., 2017).

If a very intense MCS can maintain itself until diurnal heating peaks again, then the storm can survive multiple days (Lafore *et al.*, 2017). If not, then the storm weakens and decays. Figure 11 shows the time evolution of a meridional mean of CP4 rainfall probability maps in Figure 3. We see that the rainfall probability decays through the morning, but then reappears later in the afternoon. The system appears to have continued to "propagate" westward, despite producing little to no rainfall for a period of time. This is suggestive of MCS decay and regeneration along the same track (Lafore *et al.*, 2017; Laing *et al.*, 2008, 2011).

FIGURE 11 Meridional mean of CP4 probability maps in Figure 3, but for hourly t_1 up to 23Z. $t_0 = 6Z$. [Colour figure can be viewed at wileyonlinelibrary.com]



Another interesting and relevant conceptual discussion is the existence of a relationship between storm lifetimes, diurnal cycles, and the growth of the ring pattern. The role of rotation in dampening tropospheric perturbations is determined by the Rossby radius (Ro), which is of the order of $\sim 10,000\,\mathrm{km}$ at 13°N. When considering the depth of the entire troposphere, rotational effects are insignificant on the scale of the patterns in our results, which are $\sim 1000\,\mathrm{km}$ at most. However, consider an external Rossby radius λ_R , defined as

$$\lambda_{\rm R} = \frac{\sqrt{gH\Delta\theta/\theta_0}}{f},\tag{1}$$

where g is gravitational acceleration, H is the initial depth of the cold pool, $\Delta\theta/\theta_0$ is the temperature perturbation, and f the Coriolis parameter. This defines a limit on the scale of the cold pool over timescales of $\sim 1/f$. With tropical scale $f \sim 10^{-5} \, \mathrm{s}^{-1}$ and cold-pool characteristic scales of $H \sim 10^3$ m, $\Delta \theta \sim 3$ K, and $\theta_0 \sim 300$ K, the value of λ_R is $\sim 10^6$ m. At latitudes 10–18°N, the 1/f timescale ranges between approximately 11 and 6 hours. Although temperatures recover rapidly in the interiors, the edges of large cold pools from MCS may survive longer (Tompkins, 2001), up to and beyond the 1/f timescale. The time elapsed between 6Z and peak diurnal heating is close to 1/f for those latitudes where nocturnal MCS are common, and the size order of the ringlike pattern in rainfall enhancement at 9–12 h is similar to the above calculation of λ_R . The variation of this inertial scale with *f* over the domain could also explain the "thickness" of the contributions to the composite ring pattern that result from boundary-layer interactions such as cold-pool-driven moisture convergence and lifting.

4.3 | Adaptability of the method

There is nuance to the potential conversion of these results to a statistical forecasting tool, since the probabilities shown are multiply conditional on the chosen times, locations, thresholds, and domain used to calculate them. The current method also only uses 99th percentile t_0 rainfall locations and says nothing about the relationship between location and intensity for t_0 and/or t_1 . Surpassing a given threshold of rainfall might result from different mechanisms over higher terrain, for example. We should also remember that the threshold for t_0 is not fixed here and instead changes with time of day. The rainfall probability maps in these results are analogous to a composite of binary arrays around the most intense rainfall locations in the sub-domain at t_0 . This could easily be adapted to include magnitudes in both t_0 and t_1 rainfall intensity above a given threshold, but would likely require some normalization relative to the time of day to remove the dominant diurnal signal. Including magnitude gives greater weight to the most intense rainfall events, but also adds another condition to the probability map.

The interaction of local rainfall responses and seasonal climatology is one of the main themes of investigation in tropical-scale interactions. In the current method, areas of high climatological mean rainfall appear as "smudged" stationary features at t_1 . This is because we chose to retain information about the climatological rainfall patterns as well as local links to previous rainfall. An event does not need to be anomalous to be impactful and vice versa. Given the stochastic nature of convection and the inherent difficulties in modeling its intensity on a local scale, probability of any amount of convective rain is arguably more interpretable and more useful for users of this kind

of information. Also, from a scientific perspective, we are interested in any rainfall with a meaningful physical connection to convection. For this, the actual instantaneous rate and not the anomalous rate is required. For example, a negative anomaly could still be strongly convective, but just less so than the mean and vice versa. A focus only on large local positive anomalies therefore restricts the sample of convective events.

A simple prediction tool conceivable with this method is one where a forecaster inputs the location of a storm at t_0 within a given sub-domain S, retrieves a t_1 cross-correlation between S and its wider environment from a large store of observational data and model rainfall analysis, and maps likelihoods of rainfall over a chosen threshold at t_1 given the storm's current location. Methods of this kind offer advantages over simply tracking or propagating existing features in the domain, as they incorporate information about potential interaction at distance. Crucially, this includes the relationship between existing, and new convection which tracking alone cannot capture. Of course, the robustness of such a tool requires great care and is beyond the scope of this study. A similar tool has already been developed by the NFLICS project (Anderson et al., n.d.), but here we show the potential to enhance the physical understanding of patterns using high-resolution model data alongside satellite rainfall retrievals.

While the computational simplicity of the method in this article has its merits, it is conceivable that patterns such as these could be learned with more complex machine-learning techniques with higher dimensional inputs. For example, using convolutional methods for spatial rainfall pattern learning (e.g., Badrinath et al., 2023) could yield similar results to ours, since convolutions are mathematically similar to cross-correlation. Deep learning is used increasingly for nowcasting, with models trained using satellite data (e.g., MetNet: Andrychowicz et al., 2023). However, training these models with the existing observational record alone is not ideal, due to the non-stationary nature of the climate system, both within that period and more generally (Palmer, 1999). A potential solution is to use km-scale model data to fill the sample space better. However, this requires continued evaluation of the realism of model patterns and processes; our results are an example of a pattern-based evaluation. There are also developments in hybrid approaches that combine machine learning with physical models (Das et al., 2024; Kashinath et al., 2021). Future analysis could also use methods for diagnosing cold pools explicitly from km-scale model data (e.g., Drager & Van Heever, 2017) and, supported with datasets of rainfall and identified cold pools in observations (Hoeller et al., 2024; Kirsch et al., 2024; Provod et al., 2016), use these to again predict patterns of rainfall enhancement by previous rain.

Waves and cold pools are ubiquitous and universal features of atmospheric convection, and as such the relationships shown in our results should be relevant across other tropical domains where convection dominates climatological rainfall. Similar methods could be used to explore patterns in other domains or examine the behavior of other models and their processes. For example, Mapes (2024) shows frequency composites of observed cold cloud objects in a South American domain, and the inferred spatial pattern of self-enhancement/suppression is both elliptical and dependent on the diurnal cycle. The application of the method to model fields of quantities not observable by remote sensing also presents interesting possibilities. However, the patterns produced are sensitive to model process representations, such as the parameterization of convection, and the question of whether pattern mechanisms are common between observations and models remains an important consideration.

5 | CONCLUSIONS

Our results demonstrate that lagged cross-correlations can uncover coherent structures of enhanced convective rainfall probability around early-morning rainfall events in the West African Sahel. These patterns appear in both observations and regional climate model simulations. Notably, the convection-permitting model reproduces these patterns with greater fidelity in terms of magnitude and timing, aligning more closely with satellite observations than its parameterized counterpart. The closer similarity of the observed and explicit model's pattern likely stems from an improved representation of the diurnal cycle, better representation of MCS and their life cycles, and increased sensitivity of convection to previous convection via spatially resolved nonlinear interactions such as with cold-pool gust fronts and convectively generated gravity waves.

Given the inherent unpredictability of rainfall at daily timescales in tropical regions such as the Sahel (Keane et al., 2025), there is a clear need to exploit sub-daily patterns and mechanisms to develop and evaluate models and tools that provide early warnings to vulnerable populations. This approach will become increasingly critical, as both daily and sub-daily extremes are projected to intensify in the future (Biasutti, 2019; Fitzpatrick et al., 2020; Kendon et al., 2019; Taylor et al., 2017). We expect that these efforts could be enhanced by the use of more sophisticated statistical methods than used in this article, or with machine learning. We highlight that km-scale models produce spatiotemporal patterns similar to observations, which lends credence to using the existing large volumes of model data to supplement and enhance statistical forecasts or machine-learning training datasets. Additionally, improved spatiotemporal characteristics of model rainfall at km-scale resolutions increases confidence that model processes can be evaluated with respect to observed rainfall patterns. For coarser resolutions, parameterizations need to represent either the spatial statistics or the underlying drivers. Process evaluation remains fundamental for improving forecast accuracy and constraining uncertainty in modeling of future changes.

ACKNOWLEDGEMENTS

This work was supported by the Leeds-York-Hull Natural Environment Research Council (NERC) Doctoral Training Partnership (DTP) Panorama under grant NE/S007458/, UK Met Office CASE project funding, and the LMCS project under NERC grant NE/W001888/1. All model data used were produced as an output of IMPALA (NE/M017176/1). All data analysis and computation work was done using JASMIN, the UK national collaborative facility at the Centre for Environmental Data Analysis (CEDA). We thank the members of the Leeds Cloud and Atmospheric Dynamics group for valuable discussions, and Ben Maybee for additional sharing of technical knowledge and valuable advice during the review process. We also thank three anonymous reviewers for their valuable and pragmatic comments, which have greatly improved our article. We are continually grateful to the open-source Python community for providing and maintaining the packages that made this work possible.

DATA AVAILABILITY STATEMENT

A subset of model data, including hourly precipitation, can be accessed via the CEDA Data Archive for both P25 (https://catalogue.ceda.ac.uk/uuid/4e362effa16146abbe45 c2c58f1e54ed/) and CP4 (https://catalogue.ceda.ac.uk/uuid/f46b14e670fc49cbaadf108c969e7ee0). See CP4-Africa Technical Guidelines (Senior *et al.*, 2020) for access details. GPM-IMERG is available at https://gpm.nasa.gov/data/imerg.

ORCID

James Bassford https://orcid.org/0009-0008-7940-3086

Douglas J. Parker https://orcid.org/0000-0003-2335

-8198

James Warner https://orcid.org/0000-0002-9318-8385

REFERENCES

- Anderson, S.R., Cole, S.J., Klein, C., Taylor, C.M., Diop, C.A. & Kamara, M. (2024) Nowcasting convective activity for the Sahel: a simple probabilistic approach using real-time and historical satellite data on cloud-top temperature. *Quarterly Journal of the Royal Meteorological Society*, 150(759), 597–617. Available from: https://doi.org/10.1002/qj.4607
- Andrychowicz, M., Espeholt, L., Li, D., Merchant, S., Merose, A., Zyda, F. et al. (2023) *Deep learning for day forecasts from sparse*

- observations. arXiv. Available from: https://arxiv.org/abs/2306.06079
- Badrinath, A., Monache, L.D., Hayatbini, N., Chapman, W., Cannon, F. & Ralph, M. (2023) Improving precipitation forecasts with convolutional neural networks. Weather and Forecasting, 38(2), 291–306. Available from: https://doi.org/10.1175/WAF-D-22-0002.1
- Biasutti, M. (2019) Rainfall trends in the African Sahel: characteristics, processes, and causes. *Wiley Interdisciplinary Reviews: Climate Change*, 10(4), e591. Available from: https://doi.org/10.1002/wcc.591
- Birch, C.E., Parker, D.J., Marsham, J.H., Copsey, D. & Garcia-Carreras, L. (2014) A seamless assessment of the role of convection in the water cycle of the West African Monsoon. *Journal of Geophysical Research: Atmospheres*, 119(6), 2890–2912. Available from: https://doi.org/10.1002/2013JD020887
- Birch, C.E., Parker, D.J., O'Leary, A., Marsham, J.H., Taylor, C.M., Harris, P.P. et al. (2013) Impact of soil moisture and convectively generated waves on the initiation of a West African mesoscale convective system. *Quarterly Journal of the Royal Meteorological Society*, 139(676), 1712–1730. Available from: https://doi.org/10 .1002/qj.2062
- Bony, S., Stevens, B., Frierson, D.M., Jakob, C., Kageyama, M., Pincus, R. et al. (2015) Clouds, circulation and climate sensitivity. *Nature Geoscience*, 8(4), 261–268. Available from: https://doi.org/10.1038/NGEO2398
- Cole, S.J., Anderson, S., Diop, A., Taylor, C., Klein, C., Wells, S. et al. (2022) *Nowcasting flood impacts of convective storms in the Sahel, EGU General Assembly 2022, Vienna, Austria, 23-27 May 2022, EGU22-13445*. Available from: https://doi.org/10.5194/egusphere-egu22-13445
- Colin, M., Sherwood, S., Geoffroy, O., Bony, S. & Fuchs, D. (2019) Identifying the sources of convective memory in cloud-resolving simulations. *Journal of the Atmospheric Sciences*, 76, 947–962. Available from: https://doi.org/10.1175/JAS-D-18-0036.1
- Cronin, T.W. & Wing, A.A. (2017) Clouds, circulation, and climate sensitivity in a radiative-convective equilibrium channel model. *Journal of Advances in Modeling Earth Systems*, 9(8), 2883–2905. Available from: https://doi.org/10.1002/2017MS001111
- Crook, J., Klein, C., Folwell, S., Taylor, C.M., Parker, D.J., Stratton, R. et al. (2019) Assessment of the representation of West African storm lifecycles in convection-permitting simulations. *Earth and Space Science*, 6(5), 818–835. Available from: https://doi.org/10 .1029/2018EA000491
- Das, P., Posch, A., Barber, N., Hicks, M., Duffy, K., Vandal, T. et al. (2024) Hybrid physics-AI outperforms numerical weather prediction for extreme precipitation nowcasting. NPJ Climate and Atmospheric Science, 7(1), 1–15. Available from: https://doi.org/10.1038/s41612-024-00834-8
- Drager, A.J. & Van Heever, S.C. (2017) Characterizing convective cold pools. *Journal of Advances in Modeling Earth Systems*, 9(2), 1091–1115. Available from: https://doi.org/10.1002/2016MS000788
- Droegemeier, K.K. & Wilhelmson, R.B. (1987) Numerical simulation of thunderstorm outflow dynamics. Part I: outflow sensitivity experiments and turbulence dynamics. *Journal of the Atmospheric Sciences*, 44(8), 1180–1210. Available from: https:// doi.org/10.1175/1520-0469(1987)044<1180:NSOTOD>2.0.CO;2

- Fink, A.H., Engel, T., Ermert, V., Van Der Linden, R., Schneidewind, M., Redl, R. et al. (2017) Mean climate and seasonal cycle. In: Parker, D. J. & Diop-Kane, M. (Eds.) *Meteorology of tropical West Africa*. John Wiley Sons, Ltd, pp. 1–39. Available from: https://doi.org/10.1002/9781118391297.ch1
- Fitzpatrick, R.G., Parker, D.J., Marsham, J.H., Rowell, D.P., Guichard, F.M., Taylor, C.M. et al. (2020) What drives the intensification of mesoscale convective systems over the West African Sahel under climate change? *Journal of Climate*, 33(8), 3151–3172. Available from: https://doi.org/10.1175/JCLI-D-19-0380.1
- Freitas, S.R., Grell, G.A., Chovert, A.D., Silva Dias, M.A.F. & de Lima Nascimento, E. (2024) A parameterization for cloud organization and propagation by evaporation-driven cold pool edges. *Journal of Advances in Modeling Earth Systems*, 16(1), e2023MS003982. Available from: https://doi.org/10.1029/2023MS003982
- Garcia-Carreras, L., Parker, D.J. & Marsham, J.H. (2011) What is the mechanism for the modification of convective cloud distributions by land surface-induced flows? https://doi.org/10.1175 /2010JAS3604.1
- Grandpeix, J.Y. & Lafore, J.P. (2010) A density current parameterization coupled with Emanuel's convection scheme. Part I: the models. *Journal of the Atmospheric Sciences*, 67, 881–897. Available from: https://doi.org/10.1175/2009JAS3044.1
- Haerter, J.O. (2019) Convective self-aggregation as a cold pool-driven critical phenomenon. *Geophysical Research Letters*, 46(7), 4017–4028. Available from: https://doi.org/10.1029 /2018GL081817
- Hoeller, J., Haerter, J.O. & Da Silva, N.A. (2024) Characteristics of station-derived convective cold pools over equatorial Africa. *Geophysical Research Letters*, 51(6), e2023GL107308. Available from: https://doi.org/10.1029/2023GL107308
- Hou, A.Y., Kakar, R.K., Neeck, S., Azarbarzin, A.A., Kummerow, C.D., Kojima, M. et al. (2014) The global precipitation measurement mission. *Bulletin of the American Meteorological Society*, 95(5), 701–722. Available from: https://doi.org/10.1175/BAMS-D -13-00164.1
- Houze, R.A., Jr. (2004) Mesoscale convective systems. *Reviews of Geophysics*, 42, 4. Available from: https://doi.org/10.1029/2004RG000150
- Kashinath, K., Mustafa, M., Albert, A., Wu, J.L., Jiang, C., Esmaeilzadeh, S. et al. (2021) Physics-informed machine learning: case studies for weather and climate modelling. *Philosophical Transactions of the Royal Society A: Mathematical, Physical and Engineering Sciences*, 379(2194), 20200093. Available from: https://doi.org/10.1098/rsta.2020.0093
- Keane, R.J., Parker, D.J., Dunn-Sigouin, E., Kolstad, E.W. & Marsham, J.H. (2025) Mid-latitude versus tropical scales of predictability and their implications for forecasting. *Meteorological Applications* 32(4), e70055. https://doi.org/10.1002/met.70055
- Kendon, E.J., Stratton, R.A., Tucker, S., Marsham, J.H., Berthou, S., Rowell, D.P. et al. (2019) Enhanced future changes in wet and dry extremes over Africa at convection-permitting scale. *Nature Communications*, 10(1), 1794. Available from: https://doi.org/10 .1038/s41467-019-09776-9
- Kirsch, B., Hohenegger, C. & Ament, F. (2024) Morphology and growth of convective cold pools observed by a dense station network in Germany. *Quarterly Journal of the Royal Meteorologi*cal Society, 150(759), 857–876. Available from: https://doi.org/10 .1002/qj.4626

- Klein, C. & Taylor, C.M. (2020) Dry soils can intensify mesoscale convective systems. *Proceedings of the National Academy of Sciences*, 117(35), 21132–21137.
- Lafore, J.P., Chapelon, N., Diop, M., Gueye, B., Largeron, Y., Lepape,
 S. et al. (2017) Deep convection. In: Parker, D.J. & Diop-Kane, M.
 (Eds.) *Meteorology of tropical west Africa*. Chichester: John Wiley
 & Sons, Ltd, pp. 90–129. Available from: https://doi.org/10.1002/9781118391297.ch3
- Laing, A.G., Carbone, R., Levizzani, V. & Tuttle, J. (2008) The propagation and diurnal cycles of deep convection in northern tropical Africa. *Quarterly Journal of the Royal Meteorological Society*, 134(630), 93–109. Available from: https://doi.org/10.1002/qj.194
- Laing, A.G., Carbone, R.E. & Levizzani, V. (2011) Cycles and propagation of deep convection over equatorial Africa. *Monthly Weather Review*, 139(9), 2832–2853. Available from: https://doi.org/10.1175/2011MWR3500.1
- Lane, T.P., Reeder, M.J. & Clark, T.L. (2001) Numerical modeling of gravity wave generation by deep tropical convection. *Journal of the Atmospheric Sciences*, 58(10), 1249–1274. Available from: https://doi.org/10.1175/1520-0469(2001)058<1249:NMOGWG> 2.0.CO;2
- Lin, Y.L., Deal, R.L. & Kulie, M.S. (1998) Mechanisms of cell regeneration, development, and propagation within a two-dimensional multicell storm. *Journal of the Atmospheric Sciences*, 55(10), 1867–1886. Available from: https://doi.org/10.1175/1520-0469(1998)055<1867:MOCRDA>2.0.CO;2
- Mapes, B.E. (1993) Gregarious tropical convection. *Journal of the Atmospheric Sciences*, 50(13), 2026–2037. Available from: https://doi.org/10.1175/1520-0469(1993)050<2026:GTC>2.0.CO;2
- Mapes, B.E. (2024) Evolutionary theory of convective organization. arXiv preprint. https://doi.org/10.48550/arXiv.2404.03480
- Mathon, V., Laurent, H. & Lebel, T. (2002) Mesoscale convective system rainfall in the Sahel. *Journal of Applied Meteorology*, 41(11), 1081–1092.
- Maurer, V., Bischoff-Gauß, I., Kalthoff, N., Gantner, L., Roca, R. & Panitz, H.J. (2017) Initiation of deep convection in the Sahel in a convection-permitting climate simulation for northern Africa. *Quarterly Journal of the Royal Meteorological Society*, 143(703), 806–816. Available from: https://doi.org/10.1002/qj 2966
- Meyer, B. & Haerter, J.O. (2020) Mechanical Forcing of Convection by Cold Pools: Collisions and Energy Scaling. *Journal of Advances in Modeling Earth Systems*, 12(11), e2020MS002281. Available from: https://doi.org/10.1029/2020MS002281
- Moncrieff, M.W. (2010) The multiscale organization of moist convection and the intersection of weather and climate. In: Sun, D.-Z. & Bryan, F. (Eds.) *Climate dynamics: why does climate vary?* Washington, DC: American Geophysical Union (AGU), pp. 3–26. Available from: https://doi.org/10.1029/2008GM000838
- Muller, C., Yang, D., Craig, G., Cronin, T., Fildier, B., Haerter, J.O. et al. (2022) Spontaneous aggregation of convective storms. *Annual Review of Fluid Mechanics*, 54(1), 133–157. Available from: https://doi.org/10.1146/annurev-fluid-022421-011319
- Palmer, T.N. (1999) A nonlinear dynamical perspective on climate prediction. *Journal of Climate*, 12, 575–591. Available from: https://doi.org/10.1175/1520-0442(1999)012<0575:ANDPOC> 2.0.CO;2
- Provod, M., Marsham, J.H., Parker, D.J. & Birch, C.E. (2016) A characterization of cold pools in the West African Sahel. *Monthly*

- Weather Review, 144(5), 1923–1934. Available from: https://doi.org/10.1175/MWR-D-15-0023.1
- Rasheeda Satheesh, A., Knippertz, P., Fink, A.H., Walz, E.M. & Gneiting, T. (2023) Sources of predictability of synoptic-scale rainfall during the West African summer monsoon. *Quarterly Journal of the Royal Meteorological Society*, 149(757), 3721–3737. Available from: https://doi.org/10.1002/qj.4581
- Rio, C., Hourdin, F., Grandpeix, J.Y. & Lafore, J.P. (2009) Shifting the diurnal cycle of parameterized deep convection over land. *Geo*physical Research Letters, 36, L07809. Available from: https://doi .org/10.1029/2008GL036779
- Rooney, G.G., Stirling, A.J., Stratton, R.A. & Whitall, M. (2022) C-POOL: a scheme for modelling convective cold pools in the met office unified model. *Quarterly Journal of the Royal Meteorological Society*, 148(743), 962–980. Available from: https://doi.org/10.1002/qj.4241
- Schumacher, C. & Houze, J.R. (2006) Stratiform precipitation production over sub-Saharan Africa and the tropical East Atlantic as observed by TRMM. *Quarterly Journal of the Royal Meteorological Society*, 132(620), 2235–2255. Available from: https://doi.org/10.1256/qj.05.121
- Schumacher, C., Houze, R.A. & Kraucunas, I. (2004) The tropical dynamical response to latent heating estimates derived from the TRMM precipitation radar. *Journal of the Atmospheric Sciences*, 61, 1341–1358. Available from: https://doi.org/10.1175/1520-0469(2004)061<1341:TTDRTL>2.0.CO;2
- Schumacher, R.S. & Rasmussen, K.L. (2020) The formation, character and changing nature of mesoscale convective systems. *Nature Reviews Earth and Environment*, 1(6), 300–314. Available from: https://doi.org/10.1038/s43017-020-0057-7
- Senior, C., Finney, D., Owiti, Z., Rowell, D., Marsham, J., Jackson, L., et al. (2020) *Technical guidelines for using CP4-Africa simulations data*. Zenodo: Future Climate for Africa. Available from: https://doi.org/10.5281/zenodo.4316466
- Shepherd, T.G. (2014) Atmospheric circulation as a source of uncertainty in climate change projections. *Nature Geoscience*, 7(10), 703–708. Available from: https://doi.org/10.1038/ngeo2253
- Steiner, A.K., Lackner, B.C. & Ringer, M.A. (2018) Tropical convection regimes in climate models: evaluation with satellite observations. *Atmospheric Chemistry and Physics*, 18(7), 4657–4672. Available from: https://doi.org/10.5194/acp-18-4657-2018
- Stephan, C.C., Žagar, N. & Shepherd, T.G. (2021) Waves and coherent flows in the tropical atmosphere: New opportunities, old challenges. *Quarterly Journal of the Royal Meteorological Society*, 147(738), 2597–2624. Available from: https://doi.org/10.1002/qj.4109
- Stevens, B. (2005) Atmospheric moist convection. *Annual Review of Earth and Planetary Sciences*, 33(1), 605–643. Available from: https://doi.org/10.1146/annurev.earth.33.092203.122658
- Stevens, B. & Bony, S. (2013) What are climate models missing? Science, 340(6136), 1053–1054. Available from: https://doi.org/10 .1126/science.1237554
- Stratton, R.A., Senior, C.A., Vosper, S.B., Folwell, S.S., Boutle, I.A., Earnshaw, P.D. et al. (2018) A pan-African convection-permitting regional climate simulation with the met office unified model: CP4-Africa. *Journal of Climate*, 31(9), 3485–3508. Available from: https://doi.org/10.1175/JCLI-D-17-0503.1
- Taylor, C.M., Belušić, D., Guichard, F., Parker, D.J., Vischel, T., Bock, O. et al. (2017) Frequency of extreme Sahelian storms tripled

- since 1982 in satellite observations. *Nature*, 544(7651), 475–478. Available from: https://doi.org/10.1038/nature22069
- Taylor, C.M., Gounou, A., Guichard, F., Harris, P.P., Ellis, R.J., Couvreux, F. et al. (2011a) Frequency of Sahelian storm initiation enhanced over mesoscale soil-moisture patterns. *Nature Geoscience*, 4(7), 430–433. Available from: https://doi.org/10.1038/ngeo1173
- Taylor, C.M., Harris, P.P. & Parker, D.J. (2010) Impact of soil moisture on the development of a Sahelian mesoscale convective system: a case-study from the AMMA Special Observing Period. *Quarterly Journal of the Royal Meteorological Society*, 136(S1), 456–470. Available from: https://doi.org/10.1002/qj.465
- Taylor, C.M., Klein, C., Dione, C., Parker, D.J., Marsham, J., Diop, C.A. et al. (2022) Nowcasting tracks of severe convective storms in West Africa from observations of land surface state. *Environmental Research Letters*, 17(3), 034016. Available from: https://doi.org/10.1088/1748-9326/ac536d
- Taylor, C.M., Parker, D.J., Kalthoff, N., Gaertner, M.A., Philippon, N., Bastin, S. et al. (2011b) New perspectives on land-atmosphere feedbacks from the African monsoon multidisciplinary analysis. *Atmospheric Science Letters*, 12(1), 38–44. Available from: https://doi.org/10.1002/asl.336
- Tompkins, A.M. (2001) Organization of tropical convection in low vertical wind shears: the role of cold pools. *Journal of the Atmospheric Sciences*, 58(13), 1650–1672. Available from: https://doi.org/10.1175/1520-0469(2001)058<1650:OOTCIL>2.0.CO;2
- Torri, G., Kuang, Z. & Tian, Y. (2015) Mechanisms for convection triggering by cold pools. *Geophysical Research Letters*, 42(6), 1943–1950. Available from: https://doi.org/10.1002/2015GL063227
- Trzeciak, T.M., Garcia-Carreras, L. & Marsham, J.H. (2017) Cross-Saharan transport of water vapor via recycled cold pool outflows from moist convection. *Geophysical Research Letters*, 44(3), 1554–1563. Available from: https://doi.org/10.1002/2016GL072108
- Tulich, S.N. & Kiladis, G.N. (2012) Squall lines and convectively coupled gravity waves in the tropics: why do most cloud systems propagate westward? *Journal of the Atmospheric Sciences*, 69(10), 2995–3012. Available from: https://doi.org/10.1175/JAS-D-11-0297.1
- Vizy, E.K. & Cook, K.H. (2018) Mesoscale convective systems and nocturnal rainfall over the West African Sahel: role of the Inter-tropical front. *Climate Dynamics*, 50(1-2), 587–614. Available from: https://doi.org/10.1007/s00382-017-3628-7
- Vogel, P., Knippertz, P., Gneiting, T., Fink, A.H., Klar, M. & Schlueter, A. (2021) Statistical forecasts for the occurrence of precipitation outperform global models over northern tropical Africa. *Geophysical Research Letters*, 48(3), e2020GL091022. Available from: https://doi.org/10.1029/2020GL091022

How to cite this article: Bassford, J., Parker, D.J., Marsham, J. & Warner, J. (2025) Scale interactions of deep convection in the Sahel: Exploring ring patterns in lagged cross-correlations of rainfall. *Quarterly Journal of the Royal Meteorological Society*, e70041. Available from: https://doi.org/10.1002/qj.70041